Biophysical Chemistry 154 (2011) 56–65

Contents lists available at ScienceDirect

Biophysical Chemistry

journal homepage: http://www.elsevier.com/locate/biophyschem

Two-state displacement by the kinesin-14 Ncd stalk

Mark A. Hallen, Zhang-Yi Liang, Sharyn A. Endow *

Department of Cell Biology and Structural Biology & Biophysics Program, Duke University Medical Center, Durham, NC 27710, USA

ARTICLE INFO

Article history:
Received 18 November 2010
Received in revised form 3 January 2011
Accepted 3 January 2011
Available online 13 January 2011

Keywords:
Kinesin-14 motor
Ncd
Stalk rotation
Power stroke
Nucleotide state
Microtubule binding

ABSTRACT

The nonprocessive kinesin-14 Ncd motor binds to microtubules and hydrolyzes ATP, undergoing a single displacement before releasing the microtubule. A lever-like rotation of the coiled-coil stalk is thought to drive Ncd displacements or steps along microtubules. Crystal structures and cryoelectron microscopy reconstructions imply that stalk rotation is correlated with ADP release and microtubule binding by the motor. Here we report FRET assays showing that the end of the stalk is more than ~9 nm from the microtubule when wild-type Ncd binds microtubules without added nucleotide, but the stalk is within ~6 nm of the microtubule surface when the microtubule-bound motor binds an ATP analogue, matching the rotated state observed in crystal structures. We propose that the stalk rotation is initiated when the motor binds to microtubules and releases ADP, and is completed when ATP binds.

1. Introduction

Cytoskeletal motor proteins use energy from ATP hydrolysis to produce force and move along microtubules or actin filaments, or disassemble microtubules, regulating their dynamics. How the motors do this is not well understood, but is thought to involve generation of strain by a spring-like or elastic element of the motor under load, followed by a strain-relieving step that produces force [1]. The motors are believed to undergo changes in conformation caused by changes in nucleotide binding and hydrolysis that, in turn, cause changes in motor-filament binding affinity — thus, specific states of the ATP hydrolysis cycle are postulated to generate strain and drive changes in the motor that result in motor binding to its filament, displacements or steps along the filament, and release from the filament. The structural changes of the motor are expected to be small, but, in myosin, are thought to be amplified by the relatively rigid α-helical light-chain binding region or regulatory domain, which acts like a lever arm to produce the working strokes of the motor [2–4].

Although considerable evidence now supports the hypothesis that rotation of the myosin lever arm is the primary mechanical component of the power stroke [2,5–10], less evidence is available for the kinesin motors. Two crystal structures have been reported that show the stalk of a kinesin motor in a different conformation than previous structures; both are structures of the kinesin-14 motor Ncd and exhibit the same or similar conformation [11,12] — the Ncd stalk is rotated by ~70–75°, together with one head, and the other head is unstably bound to ADP. One of the crystal structures is of a mutant that releases ADP faster than wild type [12] and the other, a mutant that binds more tightly to microtubules than wild type [11]. The altered nucleotide or microtubule binding by the mutants implies that ADP release and microtubule binding are correlated with stalk rotation. Wild-type Ncd can also be crystallized in a stalk-rotated conformation [11] although at lower resolution, possibly due to lower stability of the conformation in the absence of microtubules.

Unlike previous Ncd crystal structures with an unrotated stalk and head, the stalk-rotated structure fits well when docked into cryoelectron microscopy (cryoEM) density maps of dimeric Ncd bound to microtubules without nucleotide [13], although density corresponding to the stalk was not visible in the cryoEM reconstructions used in the dockings [11]. The stalk-rotated Ncd structures have been interpreted to resemble the motor as it releases ADP and binds to a microtubule [11,12]. Rotation of the stalk could amplify force produced by the motor, representing a power stroke. However, conflicting evidence from docking Ncd crystal structures with a rotated or unrotated stalk into other cryoEM maps has led to the proposal that the stalk rotates when the microtubule-bound motor binds ATP [14,15].

Identifying the motor conformational changes and the ATP hydrolysis state at which they occur is critical to understand how the motors work. Here we use fluorescence resonance energy transfer (FRET) assays of wild-type Ncd and a mutant that promotes stalk rotation to determine the position of the stalk relative to the microtubule in different nucleotide states of the motor.

* Corresponding author. Tel.: +1 919 684 4311; fax: +1 919 681 9929.
E-mail addresses: mark.hallen@duke.edu (M.A. Hallen), z.liang@cellbio.duke.edu (Z.-Y. Liang), endow@duke.edu (S.A. Endow).

0301-4622/$ – see front matter © 2011 Elsevier B.V. All rights reserved.
doi:10.1016/j.bpc.2011.01.001

2. Materials and methods

2.1. Plasmids and proteins

Plasmids to express EGFP-Ncd proteins in bacteria were constructed by standard methods and confirmed by DNA sequencing. EGFP-Ncd proteins for TIRF assays were partially purified by SP-Sepharose chromatography and dimer motor concentration was determined from EGFP absorbance at 489 nm ($\varepsilon = 53{,}000\ M^{-1}\ cm^{-1}$) [16].

2.2. TIRF assays

Slides and coverslips for total internal reflection fluorescence (TIRF) assays were cleaned by immersion in Piranha solution (30% H_2O_2/H_2SO_4, 1:3) [17] and sonication in deionized water or by sonication in 1 M KOH, 3 M HCl and 95% ethanol followed by sonication in deionized water. Slides were silanized in 0.15% (v/v) (3-aminopropyl)trimethoxysilane (Alfa Aesar, Ward Hill, MA) in hexane [18], rinsed in hexane, sonicated in 95% ethanol and deionized water, and stored in deionized water up to a week.

Microscope chambers were made by sealing clean coverslips onto silanized slides with double-sided tape. To immobilize microtubules on the slide, chambers were incubated with anti-α-tubulin monoclonal antibody (Chemicon International, Inc., Temecula, CA, >0.3 mg/ml) diluted 1:50 (v/v) in 0.5× PM buffer (PM buffer = 100 mM PIPES pH 6.9, 1 mM $MgSO_4$, 2 mM EGTA) + 400 nM taxol. Microtubules, either unlabeled or labeled with TMR as described below, were diluted to 100 nM (tubulin concentration) with 0.5× PM buffer + 20 μM taxol and added to the chamber.

The chamber was flushed with blocking buffer (0.5× PM buffer, 2.5 mg/ml α-casein, 2.5 mg/ml BSA, 400 nM taxol) or 1% Pluronic F-127 + 400 nM taxol in 0.5× PM buffer to prevent motor adsorption to the glass. EGFP-motor was diluted for microtubule binding (20 nM) or FRET (10 nM) assays in reaction buffer (HEM50 = 10 mM HEPES pH 7.2, 1 mM $MgCl_2$, 1 mM EGTA, 50 mM NaCl, 1 mM DTT, 1 mg/ml BSA, 400 nM taxol) without nucleotide or with 0.5 mM Mg·ADP or Mg·AMP·PNP (adenosine 5′-[β, γ-imido]triphosphate), a non-hydrolysable ATP analogue, and added to the chamber. After 1–2 min incubation, the chamber was rinsed once with reaction buffer before observation. Motor–microtubule binding in the TIRF assays was assumed to be at equilibrium so that motor binding to microtubules occurs at the same rate as dissociation from microtubules.

2.3. Rhodamine-labeled microtubules

Bovine brain tubulin was obtained from Molecular Probes, Inc. (Eugene, OR) covalently labeled with TMR to a stoichiometry of 2.6 moles TMR/moles α,β-tubulin dimer. The labeling was performed by incubation of microtubules with *N*-hydroxy succinimidyl 5-carboxytetramethylrhodamine ester, followed by two cycles of polymerization–depolymerization [19,20]. Bovine brain α,β-tubulin dimers contain 34 lysines distributed essentially randomly on the surface. The activated succinimidyl TMR esters are thought to label random surface lysines [20]. Because the labeling was done on microtubules rather than tubulin, the TMR fluorophores are expected to be predominantly on the outer microtubule surface rather than lumen. Purification of the labeled tubulin through two assembly–disassembly cycles ensures that the TMR-tubulin is competent to assemble into microtubules. TMR-microtubules for TIRF binding assays and FRET assays were assembled from 10 μM TMR-tubulin + 30 μM unlabeled porcine brain tubulin (1:3).

2.4. TIRF microscopy

Time-lapse images were acquired at 22 °C using a prism-based TIRF microscope custom-built on a Zeiss Axioskop 2FS microscope (Thornwood, NY) equipped with a Zeiss 100×/1.45 NA Plan-Fluar oil immersion objective. Specimen excitation was by the 488-nm line of an Ar laser (Melles Griot, Carlsbad, CA, Model 532-MAP-A01) measured at ~0.4 mW before the prism. Images were recorded with an Andor iXon 897 EM-CCD camera (Belfast, UK) driven by Andor iXon v 4.4.0.0 software at a gain of 300, 250 ms exposure time and 1 s/frame. GFP and rhodamine/FRET fluorescence was collected with 510/30BP and 620/50BP emission filters (Chroma Technology Corp., Rockingham, VT), respectively. A beamsplitter with 510/30BP, 565DCLP and 650/75BP filters was used in microtubule-binding assays for simultaneous collection of GFP and rhodamine images.

2.5. TIRF data analysis

Microtubule fluorescence was measured by manually tracking the time-lapse images using ImageJ v 1.38t (NIH, Bethesda, MD). Nonspecific fluorescence in the images was subtracted from the microtubule fluorescence to correct for background. Because of the difference in emission filter and motor concentration, GFP bleed through into the rhodamine/FRET channel was determined in separate controls for the microtubule-binding and FRET assays using unlabeled microtubules (100 nM) and the corresponding motor concentration (20 nM EGFP-motor for microtubule-binding assays or 10 nM EGFP-motor for FRET assays). Bleed-through fluorescence was determined to be ~11–16% of the GFP fluorescence in microtubule-binding assays of the EGFP-motors without nucleotide; it was subtracted from the rhodamine fluorescence before determining the ratios between the GFP and rhodamine fluorescence. For the FRET assays, bleed-through fluorescence was found to be negligible — only ~2–3% or less of the GFP fluorescence appeared in the rhodamine/FRET channel in control assays with unlabeled microtubules; the FRET data were therefore not corrected for GFP bleed through.

Mean fluorescence from several FRET assays was averaged and normalized, then fit to

$$f(t) = m3 + m2\ e^{-m1*t} \tag{1}$$

where f(t) = fluorescence at t = time (s), m2 = total fluorescence lost and m3 = fluorescence at t = ∞ to determine a photobleaching rate constant, m1 = k_{PB}. Donor quenching and acceptor sensitization effects were determined by comparing photobleaching rate constants for the donor or acceptor alone, and with each other under the same nucleotide conditions. For the acceptor photobleaching experiments, m3 was assumed to be 0; the microtubules are expected to photobleach without recovery as t goes to infinity, given that the TMR fluorophores are covalently bound to tubulin and photobleaching recovery would require assembly of TMR-tubulin into microtubules.

2.6. FRET calculations and modeling

The EGFP-Ncd emission spectrum, f(λ), at $\lambda_{ex} = 400$ nm and $\lambda_{em} = 420$–600 nm and TMR-tubulin absorbance spectrum, E(λ), at $\lambda_{ex} = 400$–600 nm and $\lambda_{em} = 620$ nm were read in a Varian Cary Eclipse fluorimeter, normalized and used to calculate the overlap integral, J, the overlap between the donor emission spectrum and acceptor absorbance spectrum, and the Förster distance, R_0, the distance at which the FRET efficiency for the EGFP-Ncd (donor) and TMR-microtubule (acceptor) FRET pair is 50% [21,22]. The overlap integral, J, was calculated from the wavelength λ by normalizing the EGFP emission spectrum f(λ) and TMR absorbance spectrum E(λ) such that

$$\int_{420\ nm}^{600\ nm} f(\lambda)d\lambda = 1 \quad \text{and} \quad \max_{\lambda} E(\lambda) = 1. \tag{2}$$

The integral from 0 to infinity was approximated from the spectral integral from 420–600 nm since f(λ)E(λ) is ~0 outside that range. Integration was performed numerically by a weighted sum of points approximately 1 nm apart in λ, then J was calculated by

$$J = \int_{420\ \mathrm{nm}}^{600\ \mathrm{nm}} f(\lambda)E(\lambda)\lambda^4 d\lambda = 2.3 \times 10^{10}\ \ \mathrm{nm}^4 \tag{3}$$

The Förster distance, R_0, is given by

$$R_0 = \left(\frac{(9\times ln10)\kappa^2 Q_D \varepsilon_A J}{4(2\pi)^5\ N n^4}\right)^{1/6} = \left(\frac{\left(8.786\times10^{-11}\ \ \mathrm{M\ cm\,nm^2}\right)\kappa^2 Q_D \varepsilon_A J}{n^4}\right)^{1/6} = 5.40\ \mathrm{nm} \tag{4}$$

[22]. The index of refraction, n, was taken to be 1.33; the donor quantum yield, Q_D, 0.60 [16]; the maximal acceptor molar absorptivity, ε_A, 95 000 $M^{-1}\ cm^{-1}$ [23]; and the dipole alignment constant, κ^2, 2/3, indicating random alignment of the two fluorophores [21]; N is Avogadro's number.

The FRET efficiency versus the distance between EGFP-Ncd and randomly-labeled TMR-microtubules was calculated from the geometry of the motor bound to a microtubule (see below). The efficiency of energy transfer in FRET assays was calculated from the donor photoquenching, determined from the photobleaching rate constant of the donor with and without the acceptor:

$$E = 1 - \frac{k_{PB,D+A}}{k_{PB,D-A}} \tag{5}$$

to estimate the distance between the EGFP-motor and microtubule surface [24]. Note that the photobleaching decay rate is the reciprocal of the time constant used to quantify the rate of photobleaching. The GFP-microtubule distance was calculated numerically from the efficiency using the MATLAB routine *fzero*.

The randomness of TMR-tubulin incorporation into microtubules was tested by measuring fluorescence along the length of TMR-microtubules (62.5-nm wide rectangles) in TIRF images (fields, n = 3; microtubules, n = 9); relative differences in mean fluorescence between adjacent rectangles were calculated and compared to background (fields, n = 3; background regions, n = 9). The comparisons yielded overlapping values for the microtubules and background, indicating that the microtubule fluorescent labeling at the nm to μm level is not significantly less random than background fluorescence.

2.7. FRET theoretical analysis

The nucleotide state in which the Ncd stalk rotates was determined by measuring the distance from the stalk to the microtubule under different nucleotide conditions by FRET between EGFP at the end of the stalk (donor) and randomly-labeled TMR-microtubules (acceptor). The use of a randomly-labeled acceptor differs from the specifically-labeled donor and acceptor standardly used in FRET assays, although others have previously deviated from this convention, e.g., by using a multiply-labeled donor and randomly-labeled acceptor [25]. The FRET efficiency between an EGFP-motor and randomly-labeled TMR-microtubule was calculated from the geometry of a motor bound to a microtubule using a method analogous to Baird et al. [25]. The Förster distance, R_0, of a donor–acceptor pair is defined such that for a given excited donor, the rate constant for resonance energy transfer, k_t, to a given acceptor is

$$k_t = k_f\left(\frac{R_0^6}{r^6}\right) \tag{6}$$

where r is the distance from the donor to the acceptor and k_f is the fluorescence emission rate constant for the donor. The overall energy transfer rate is the sum of the transfer rates to all available acceptors. Thus, the average transfer rate constant for a donor is $k_f R_0^6$ times the average sum of r^{-6} for all acceptors. We can neglect acceptors on different microtubules than the donor, as microtubules were almost always >1 μm apart; transfer efficiencies to these other microtubules would be on the order of $200^{-6} \approx 10^{-14}$ or less. The TMR acceptors are on average randomly distributed on the surface of a microtubule, with n_L acceptors per nanometer of microtubule length. In our case, $n_L = 13*2.6/(4*8\ \mathrm{nm}) = 1.056\ \mathrm{nm}^{-1}$ for a 13-protofilament microtubule of 8-nm tubulin dimers with 1 in 4 dimers labeled, each with an average of 2.6 TMR molecules. Points on the surface of a microtubule can be identified by a length coordinate z, with z = 0 at the donor, and an angle coordinate θ around the microtubule, with θ = 0 aligned with the donor. The average transfer rate constant $\langle k_t \rangle$ is then

$$\langle k_t \rangle = k_f R_0^6 \frac{n_L}{2\pi} \int_{-\infty}^{\infty} \int_0^{2\pi} \frac{1}{d(z,\theta)^6} d\theta dz \tag{7}$$

where d denotes the distance from the donor to the point at (z,θ) on the surface of the microtubule; the factor of 1/2π is due to the fact that the acceptor density is given only per unit length, while the integral is taken over both length and angle. The two EGFPs at the end of the stalk of the dimeric motor are assumed to dimerize due to their close proximity, but dimerization of the donor is unlikely to affect the energy transfer efficiency unless the acceptor is saturated.

d(z,θ) can be calculated using the Pythagorean theorem, as the distance has a component parallel to the microtubule (length |z|) and one perpendicular to it. This latter component depends on the distance h of the donor from the microtubule. The law of cosines gives the perpendicular component of the distance as

$$\left((h + r_{MT})^2 + r_{MT}^2 - 2(h + r_{MT}) r_{MT}\ cos\theta\right)^{1/2} \tag{8}$$

where r_{MT} is the microtubule radius of ~12.5 nm, thus

$$\frac{\langle k_t \rangle}{k_f} = R_0^6 \frac{n_L}{2\pi} \int_{-\infty}^{\infty} \int_0^{2\pi} \frac{d\theta dz}{\left(z^2 + (h + r_{MT})^2 + r_{MT}^2 - 2(h + r_{MT}) r_{MT}\ cos\theta\right)^3}. \tag{9}$$

The integral over angle can be performed analytically; letting $q = h^2 + 4hr_{MT} + 4r_{MT}^2$,

$$\frac{\langle k_t \rangle}{k_f} = R_0^6 \frac{n_L}{8} \int_{-\infty}^{\infty} \frac{3\left(h^2 + z^2\right)^2 + 2\left(h^2 + z^2\right)\left(q + z^2\right) + 3\left(q + z^2\right)^2}{\left(h^2 + z^2\right)^{5/2}\left(q + z^2\right)^{5/2}} dz. \tag{10}$$

The efficiency can then be calculated by

$$E = \frac{1}{1 + \left(\frac{r}{R_o}\right)^6} = \frac{1}{1 + \frac{k_f}{k_t}} \quad \text{or} \quad E = \frac{1}{1 + \frac{k_f}{\langle k_t \rangle}} \tag{11}$$

for single or multiple acceptors, respectively.

2.8. FRET error analysis

Lower than expected incorporation of TMR-tubulin into the microtubules would decrease the distances estimated from our donor quenching assays, but only slightly; for example, incorporation at 50% of the expected ratio was calculated to decrease the distances by ~1 nm. Errors in the donor quenching assays due to photobleaching recovery would also be small. In a system with rapid recovery of

unbound fluorophores, a dissociation rate constant k_{off} for bound fluorophores, and a first-order rate constant k_{PB} for photobleaching, the fluorescence due to bound fluorophores would be given by

$$\frac{k_{PB}e^{-(k_{off}+k_{PB})t}+k_{off}}{k_{PB}+k_{off}} \tag{12}$$

where k_{off} is not significantly different in the presence or absence of the acceptor. Because most (>75%) of the fluorescence was lost over time in the background-corrected assays, $k_{off}<<k_{PB}$. This indicates that the exponential decay constant m1 is a good measure of k_{PB} (within ~25%, with the photobleaching recovery error being the same for the donor alone and donor + acceptor assays). Photobleaching recovery errors would thus not result in misleading apparent donor quenching or lack of donor quenching; furthermore, errors in the GFP-microtubule distance measurements are estimated to be well under a nanometer.

Errors from nonrandom labeling by TMR of lysines are also expected to be well under a nanometer; this was estimated by calculating FRET efficiency using the summation (rather than integral) form of Eq. (7),

$$\langle k_t\rangle = k_f R_0^6 \sum_{lys} \frac{p(lys)}{d\left(z_{lys},\theta_{lys}\right)^6} \tag{13}$$

where the sum is over all lysines on the surface of the microtubule, p (lys) is the probability of a given lysine being TMR-labelled, and z_{lys} and θ_{lys} are the coordinates of that lysine. If one assumes that labeled tubulin subunits incorporate randomly into the microtubule, then p (lys) is the same for each lysine on a given subunit and its equivalent on all other subunits in the microtubule, so Eq. (13) can be expressed as a sum over the lysines on an individual subunit,

$$\langle k_t\rangle = k_f R_0^6 \sum_{i=-\infty}^{\infty}\sum_{j=0}^{12}\sum_{lys(1\ subunit)} \frac{p(lys)}{d\left(z_{lys}+(8\ \text{nm})i,\theta_{lys}+\left(\frac{2\pi}{13}\right)j\right)^6} \tag{14}$$

and the FRET efficiency E can be calculated from $<k_t>/k_f$ using Eq. (11), just as in the integral case. In the worst-case scenarios of all TMR moieties lying as close to or as far away from the GFP as possible, errors in distance for the FRET efficiencies that we observed were <1 nm. Calculations based on all the TMR moieties being in the lumen rather than on the surface of the microtubule resulted in the distance h being reduced by ~4 nm; however, we consider this possibility to be unlikely, and, in addition, the closer distances would not change our interpretation that the stalk undergoes displacement in two nucleotide states.

2.9. Effect of initial stalk position on step size

Previous cryoEM density maps [14,15] have been interpreted to show the stalk of the Ncd motor tilted toward the microtubule plus end when the motor is bound to the microtubule in the no-nucleotide state. This tilt causes a small increase in step size relative to the size it would be starting from a vertical position, depending on the angle of tilt. If the stalk is tilted toward the microtubule plus end by an angle θ_1, it will rotate to a vertical position and continue to rotate toward the microtubule surface through an angle θ_2. The step size from the rotation $\theta_r=\theta_1+\theta_2$ is

$$l(\sin\theta_1+\sin\theta_2) \tag{15}$$

where l = stalk length. The stalk of full-length Ncd is ~20.2 nm in length, based on the coiled-coil region predicted from the protein sequence (V208-R346, 139 residues) and the length of a truncated coiled-coil stalk in an Ncd crystal structure (M292-R346, 55 residues ≈8 nm, PDB 1N6M) [11].

An initial tilt towards the plus end [14,15], measured as ~46° from Supplementary Fig. 3 of Endres et al. (2006) [15], would give a step size of 33.5 nm, if the stalk rotates to a vertical position and then continues to rotate an additional 70° to place the end of the stalk ~6 nm from the microtubule surface ($\theta_r=46°+70°=116°$), assuming that the rotation occurs in a plane parallel to the microtubule long axis.

2.10. Step size in laser-trap assays

A single-molecule study of full-length Ncd by laser-trap assays reported steps of ~1–2 nm and ~9 nm [26]. These steps are smaller than the 19-nm displacement predicted for a 70° rotation of the stalk from a vertical position relative to the microtubule ($\theta_1=0$, $\theta_2=70°$), based on a 20.2-nm stalk length for full-length Ncd (see above). The 19-nm displacement was found by solving $\sin 70° = d/(20.2\ \text{nm})$ for d, assuming that the stalk starts vertical to the microtubule and rotates in a plane parallel to the microtubule long axis, as shown:

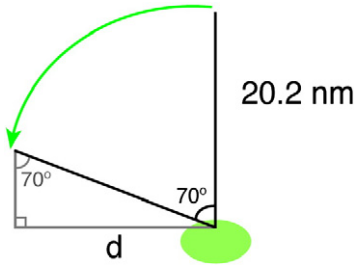

The angle corresponding to a step of d = ~9 nm was calculated by $\sin\theta_2 = 9\ \text{nm}/(20.2\ \text{nm})$ to obtain $\theta_2=$~26°. The step size also depends on the initial tilt of the stalk towards the microtubule plus (or minus) end, as noted above; an initial tilt of the motor towards the plus end would increase the step size, depending on the angle of tilt.

3. Results

3.1. Stalk rotation mutants

An unanswered question regarding the kinesin motor mechanism is the nucleotide state(s) in which force is produced. The report of a crystal structure in which the stalk of the kinesin-14 motor Ncd is rotated by ~75° relative to previous crystal structures [11] led to the hypothesis that the stalk functions like a lever arm to amplify small movements of the motor. To determine the nucleotide state or states in which the stalk rotates, we tested wild-type Ncd and an Ncd mutant, that was crystallized in a stalk-rotated conformation, NcdN600K, in microtubule-binding and FRET assays by total internal reflection fluorescence (TIRF) microscopy.

The NcdN600K mutant motor was identical to wild type except for a single amino acid change in the microtubule-binding site. The wild-type and mutant motors both contained EGFP at the N terminus of the stalk (H293-R346) followed by the motor domain (N348-K700) (Fig. 1). NcdN600K binds more tightly to microtubules than wild type [27] and, when crystallized, showed a large, ~75° rotation of the stalk with a pivot point at G347 [11], differing from previous Ncd structures (Fig. 2). The reason the NcdN600K motor crystallized in the stalk-rotated conformation is not certain, but may be related to the slightly unstable ADP binding compared to wild type and tight binding by the mutant to microtubules, which may facilitate stalk rotation under the crystallization conditions used. One of the two heads in the NcdN600K

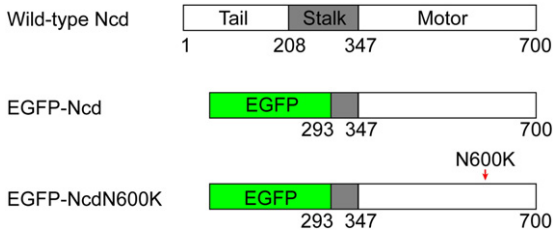

Fig. 1. Wild-type and mutant Ncd motors. Wild-type Ncd consists of a basic, proline-rich tail, α-helical coiled-coil stalk with a pivot point of rotation at G347, and conserved motor domain (top). The wild-type and NcdN600K mutant motors used in microtubule-binding and FRET assays contained EGFP (M1-K239) fused to the N terminus of the stalk (H293-R346) followed by the motor domain (N348-K700). The mutant contained N600K in the motor microtubule-binding site (bottom).

crystal structure interacts extensively with the stalk and rotates with the stalk, but the other head shows disrupted interactions with the stalk, allowing the stalk to rotate.

3.2. Microtubule binding by Ncd and the NcdN600K mutant

Microtubule-binding assays with Ncd are difficult to perform accurately because the motor can readily aggregate without binding to microtubules in standard pelleting assays. Directly imaging the EGFP-motors bound to microtubules labeled with tetramethylrhodamine (TMR) overcomes the problem of correcting for pelleted but unbound motor, and allows measurements of microtubule binding under the conditions of our FRET assays. We therefore tested the EGFP-labeled wild-type and NcdN600K mutant motor for microtubule binding by TIRF microscopy by exciting at 488 nm and simultaneously recording GFP and rhodamine fluorescence.

The assays showed TMR-microtubules without motor in the rhodamine channel due to excitation by 488-nm light ($n \approx 400$; fields, $n = 51$) (Fig. 3A, bottom). Assays with EGFP-motors and TMR-microtubules showed fluorescence signals in both the GFP and rhodamine channels. Wild-type EGFP-Ncd was bound to microtubules without nucleotide or with AMP·PNP, but not with ADP, consistent with previous findings that no nucleotide and ATP are strong binding states of the kinesin motors and ADP is a weak-binding state [28,29]. EGFP-NcdN600K was bound to microtubules with or without nucleotide, exhibiting high microtubule-binding affinity, even with ADP, as reported previously [27].

To quantitate binding by the motors, GFP and rhodamine dual images of the wild-type or mutant EGFP-motor bound to TMR-microtubules without nucleotide, recorded by TIRF microscopy, were corrected for background and bleed through of GFP fluorescence into the rhodamine channel, and the ratio of GFP/rhodamine fluorescence was determined. Fluorescence ratios were comparable for wild-type EGFP-Ncd (0.68 ± 0.04) and EGFP-NcdN600K (0.7 ± 0.2) without nucleotide (Fig. 3B), indicating similar microtubule-binding affinity.

3.3. FRET assays of stalk movement

To detect movement of the stalk, we performed FRET assays by TIRF microscopy with the wild-type or mutant EGFP-motor as donor and TMR-microtubules as acceptor. Slides were excited at the donor

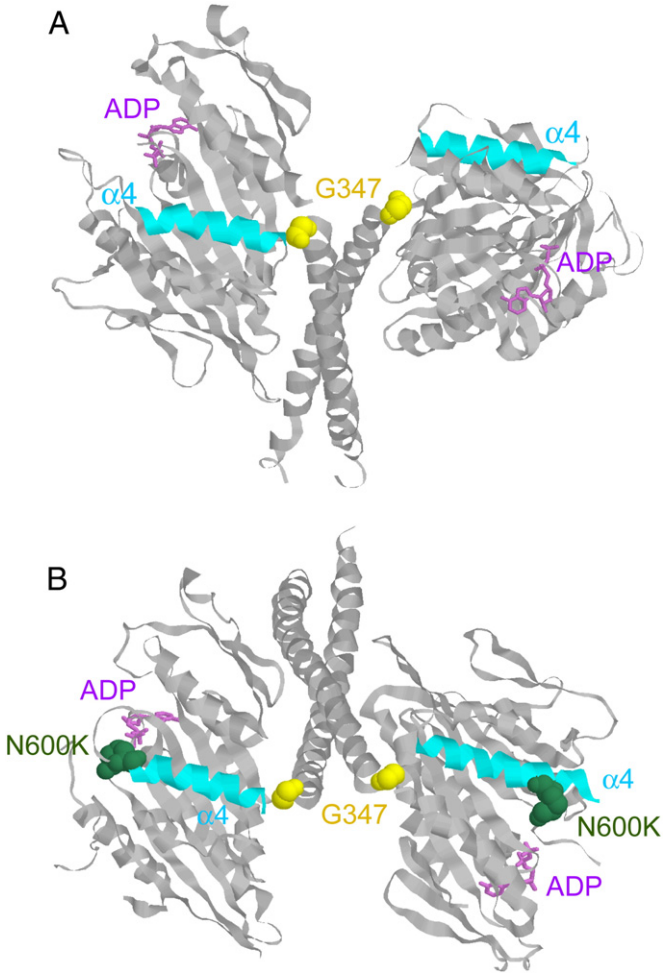

Fig. 2. Wild-type and NcdN600K mutant motors. Crystal structures of (A) wild-type Ncd (PDB 2NCD) and (B) NcdN600K (PDB 1N6M) with the stalk and one head (right) rotated relative to the other head (left). The heads on the left in A and B are aligned to show the stalk/head rotation. The pivot point of stalk rotation is G347 (yellow). NcdN600K (dark green) in helix α4 (cyan) of the microtubule-binding site causes the motor to bind tightly to microtubules. ADP, violet.

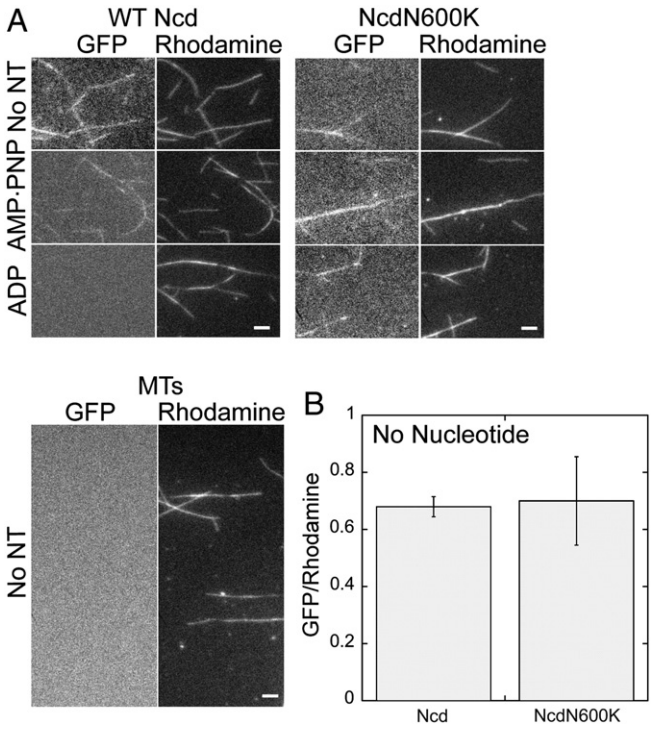

Fig. 3. Microtubule-binding assays by TIRF microscopy. (A) Wild-type EGFP-Ncd (left) and EGFP-NcdN600K (right) bound to microtubules with no nucleotide, AMP·PNP or ADP. Microtubules without motor (bottom). Dual GFP (510/30BP) and rhodamine (650/75BP) images of the same fields with excitation at 488 nm. Bars, 4 μm. (B) GFP/rhodamine fluorescence ratios of the wild-type and NcdN600K EGFP-motors bound to TMR-microtubules without nucleotide, corrected for background and bleed through of GFP into the rhodamine channel.

excitation wavelength and rhodamine/FRET or GFP fluorescence was recorded over time in acceptor photobleaching assays or donor quenching assays, respectively. Energy transfer from the donor to the acceptor is expected to occur when the EGFP-motor is in close proximity to the TMR-microtubule; the FRET efficiency is expected to vary with the distance between the EGFP-motor and randomly-labeled TMR-microtubule. We calculated the relationship between FRET efficiency and the distance of the EGFP to a TMR fluorophore from the geometry of the motor bound to a microtubule (Fig. 4), using a method analogous to one reported previously [25]. Theoretical calculations of the Förster distance, R_0, the distance at which the FRET efficiency for the EGFP and TMR donor–acceptor FRET pair is 50%, gave $R_0 = 5.4$ nm.

Energy transfer from the donor to the acceptor is expected to increase the rate of acceptor photobleaching and decrease the rate of donor quenching, which can be used to establish the occurrence of FRET.

3.4. Acceptor photobleaching FRET assays

We performed acceptor photobleaching assays by exciting at the donor excitation wavelength, 488 nm, and recording rhodamine/FRET fluorescence over time. The data were analyzed for an increase in the acceptor photobleaching rate in the presence of the donor. The rhodamine/FRET signal arises from 488-nm excitation of the TMR-microtubules and by FRET caused by EGFP-motor interactions with the microtubules; faster fluorescence decay of EGFP-motor-bound TMR-microtubules compared to TMR-microtubules was attributed to faster photobleaching of the acceptor in the presence of the donor due to energy transfer.

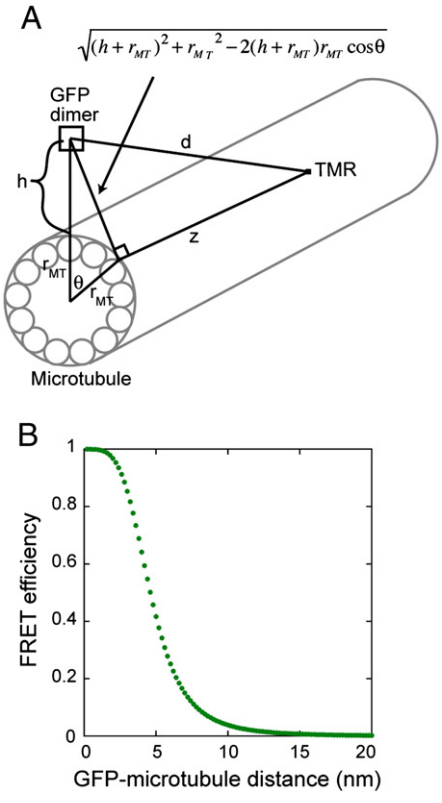

Fig. 4. FRET model. (A) Model for energy transfer between a GFP-labeled motor and randomly-labeled TMR-microtubule. r_{MT}, microtubule radius; h, distance of the GFP from the microtubule surface. (B) FRET efficiency versus GFP-microtubule distance (h) calculated from the model.

The rhodamine/FRET fluorescence in the TIRF image sequences was corrected for background fluorescence, data from several assays were averaged and normalized, and mean fluorescence was plotted versus time (Fig. 5A). The curves were fit to Eq. (1) (Materials and methods) with $m3 = 0$ at $t = \infty$ to obtain photobleaching rate constants. Note that the curve fits to data from time-lapse sequences give rate constants that are less error-prone than values obtained from individual images or data points.

As controls, we first measured photobleaching rate constants for TMR-microtubules with different nucleotides, but without EGFP-motor (Fig. 5A). TMR-microtubules showed a rhodamine fluorescence signal that decreased over time with a rate constant of $0.00182 \pm 0.00002\ s^{-1}$ without nucleotide and $0.00090 \pm 0.00003\ s^{-1}$ with AMP·PNP, but there was no measurable decrease with ADP (Table 1). These differences in acceptor photobleaching rate constants with no nucleotide or different nucleotides were not expected, but could arise from a number of different factors including nucleotide reactivity with oxygen species that cause bleaching. The appropriate control for each assay in Table 1 is therefore the TMR-MTs with the corresponding nucleotide but without the wild-type or mutant EGFP-motor. The values were compared with the rate constants for EGFP-motor bound to TMR-microtubules with no nucleotide, AMP·PNP or ADP to determine whether the donor causes an increase in acceptor photobleaching, as expected if energy transfer were occurring.

TMR-microtubules with bound wild-type EGFP-Ncd showed a rhodamine/FRET signal that decreased over time in assays with no nucleotide ($0.00176 \pm 0.00005\ s^{-1}$) or with AMP·PNP ($0.00100 \pm 0.00003\ s^{-1}$) (Fig. 5A, Table 1). The rate constant with AMP·PNP was slightly higher than microtubules without motor, providing evidence for FRET, but it was not significantly different with no nucleotide. Assays with ADP showed no motor bound to the microtubules ($n = 10$).

The rhodamine/FRET signal for TMR-microtubules with bound EGFP-NcdN600K decayed more rapidly than TMR-microtubules alone, either without nucleotide ($0.00210 \pm 0.00004\ s^{-1}$) or with AMP·PNP ($0.00206 \pm 0.00003\ s^{-1}$) or ADP ($0.00191 \pm 0.00003\ s^{-1}$) (Fig. 5A, Table 1). These data show energy transfer in all three nucleotide states of the EGFP-NcdN600K motor that were tested, including ADP, the weak-binding state of the kinesin motors [28,29].

The acceptor photobleaching assays indicate that FRET between wild-type EGFP-Ncd and TMR-microtubules occurs in the ATP-like state, but not in the no nucleotide or ADP state. They further show that FRET occurs in all three nucleotide states of the EGFP-NcdN600K motor. EGFP-NcdN600K is trapped in a stalk-rotated conformation and binds tightly to microtubules, and shows FRET with or without nucleotide, including ADP.

3.5. Donor quenching FRET assays

The FRET signal in the TIRF assays is critically dependent on background fluorescence, which could mask a low signal. Because of this, we also tested wild-type EGFP-Ncd and EGFP-NcdN600K for energy transfer by measuring photobleaching of the donor with and without the acceptor. Slower donor photobleaching, or donor quenching, is expected to occur in the presence of the acceptor if energy transfer is occurring. Donor quenching is a reliable indicator of FRET because of the absence of acceptor fluorescence bleed through into the GFP channel. The donor fluorescence bleed through into the rhodamine/FRET channel in our acceptor photobleaching assays was negligible — ~2–3% or less of the GFP fluorescence in control assays with unlabeled microtubules — but higher bleed through could contribute to the rhodamine/FRET fluorescence and mask the FRET signal. We first determined the fluorescence decay rates of wild-type EGFP-Ncd and EGFP-NcdN600K in TIRF assays without acceptor using unlabeled microtubules, then performed assays with EGFP-motor bound to TMR-labeled microtubules. For both the donor alone and

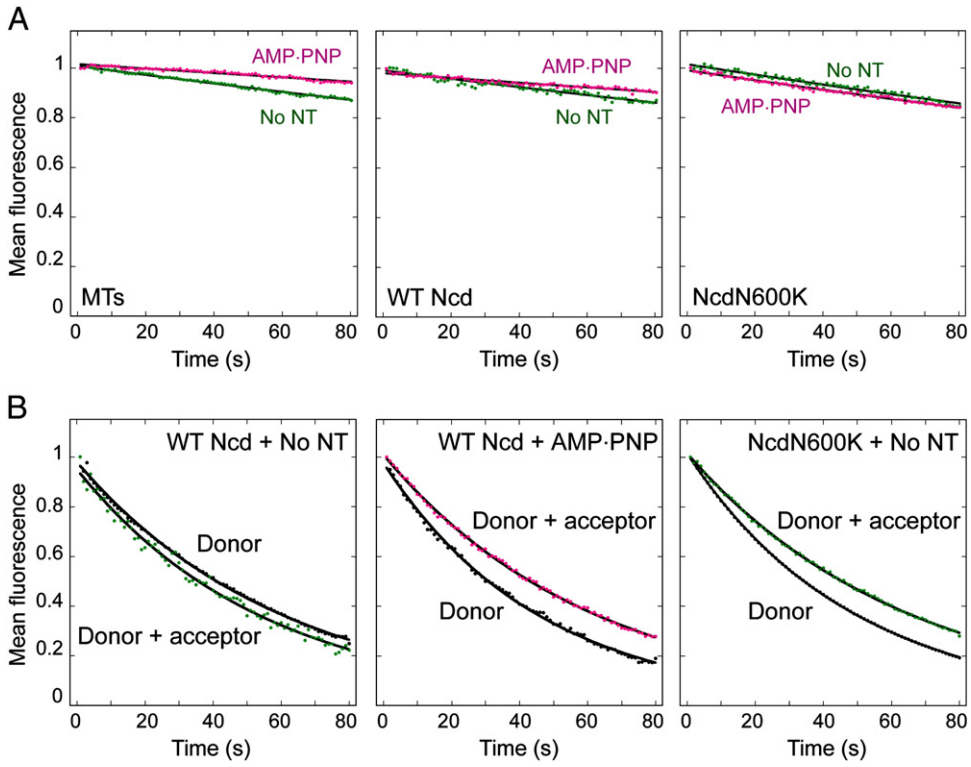

Fig. 5. FRET assays of stalk movement. (A) Acceptor photobleaching assays. Rhodamine/FRET signal (620/50BP, $\lambda_{ex} = 488$ nm) over time. TMR-microtubules without motor (left); wild-type Ncd (middle) or NcdN600K (right) with TMR-microtubules. No nucleotide (green); AMP·PNP (magenta). (B) Donor quenching assays. GFP signal (510/30BP, $\lambda_{ex} = 488$ nm). EGFP-motor with unlabeled microtubules (donor, black) or TMR-microtubules (donor + acceptor). No nucleotide (green); AMP·PNP (magenta). Wild-type EGFP-Ncd with no nucleotide (left) or AMP·PNP (middle); EGFP-NcdN600K with no nucleotide (right). Mean fluorescence normalized to m2 + m3 = 1 at t = 0 and m3 = 0 at t = ∞.

Table 1
Acceptor photobleaching assays.

Motor	No nucleotide (s^{-1})	AMP·PNP (s^{-1})	ADP (s^{-1})
TMR-MTs	0.00182 ± 0.00002	0.00090 ± 0.00003	No measurable decay
TMR-MTs + EGFP-Ncd	0.00176 ± 0.00005	0.00100 ± 0.00003	No binding (n = 10)
TMR-MTs + EGFP-NcdN600K	0.00210 ± 0.00004	0.00206 ± 0.00003	0.00191 ± 0.00003

Rhodamine/FRET fluorescence (620/50BP) over time with or without donor EGFP-motor, corrected for background, averaged and fit to Eq. (1) to determine $m1 = k_{PB}$. No binding, no detectable GFP fluorescence before or after TMR-microtubule time-lapse imaging. MTs, microtubules.

donor with acceptor, GFP fluorescence was recorded over time (Fig. 5B).

Like the acceptor photobleaching assays, the assays of the wild-type or mutant EGFP-Ncd motor with unlabeled microtubules showed differences with no nucleotide or AMP·PNP that we attributed to different nucleotide environments (Table 2). The appropriate control for each assay is therefore the EGFP-motor with unlabeled microtubules and the corresponding nucleotide. Fluorescence over time of wild-type EGFP-Ncd with no nucleotide bound to unlabeled microtubules or the slide surface did not differ from one another; the data were therefore averaged, giving a decay rate constant of $0.0164 \pm 0.0005\ s^{-1}$ for the donor without acceptor. Assays of EGFP-Ncd with acceptor TMR-microtubules and no nucleotide gave $0.018 \pm 0.001\ s^{-1}$, almost overlapping the rate constant for the donor alone, showing little difference in the donor photobleaching rate constant with or without the acceptor (Fig. 5B, Table 2). By contrast, assays of EGFP-Ncd with AMP·PNP gave a photobleaching rate constant of $0.0217 \pm 0.0006\ s^{-1}$ without acceptor and $0.0163 \pm 0.0004\ s^{-1}$ with acceptor. The significantly lower rate constant in the presence of the acceptor indicates that energy transfer from the donor to the acceptor occurs when wild-type EGFP-Ncd is bound to TMR-microtubules with AMP·PNP.

We also tested the EGFP-NcdN600K motor in donor quenching assays without nucleotide to confirm the effects observed for wild-type Ncd with TMR-microtubules and AMP·PNP. EGFP-NcdN600K showed FRET in acceptor photobleaching assays under all three nucleotide conditions tested and thus was expected to show FRET in

Table 2
Donor quenching assays.

Motor	No nucleotide(s^{-1})	E (%)	H (nm)	AMP·PNP (s^{-1})	E (%)	H (nm)
EGFP-Ncd + unlabeled MTs	0.0164 ± 0.0005			0.0217 ± 0.0006		
EGFP-Ncd + TMR-MTs	0.018 ± 0.001	<~5	>~9	0.0163 ± 0.0004	24.9	6
EGFP-NcdN600K + unlabeled MTs	0.02055 ± 0.00007			ND		
EGFP-NcdN600K + TMR-MTs	0.0155 ± 0.0003	24.6	6	ND		

EGFP-motor fluorescence (510/30BP) over time with unlabelled microtubules or TMR-microtubules, corrected for background, averaged and fit to Eq. (1) to determine $m1 = k_{PB}$. Energy transfer efficiency, E, from Eq. (5). Distance between EGFP and TMR-microtubule, h, from Eqs. (10) and (11). MTs, microtubules. ND, not determined.

donor quenching assays. Assays of EGFP-NcdN600K with no nucleotide and without acceptor gave a photobleaching rate constant of $0.02055 \pm 0.00007\ s^{-1}$, whereas assays with acceptor gave a rate constant of $0.0155 \pm 0.0003\ s^{-1}$ (Fig. 5B, Table 2). The significantly lower rate constant in the presence of acceptor provides evidence that energy transfer from the donor to acceptor occurs when EGFP-NcdN600K is bound to TMR-microtubules without nucleotide, consistent with the acceptor photobleaching assays. The differences in rate constants strongly support our interpretation that the fluorescence decreases are due to photobleaching whose rate is influenced by FRET, rather than simply dissociation of the motor from the microtubule. In the latter case, the addition of acceptor would not be expected to affect the rate constant — if it showed any effect, it might be expected to increase, rather than lower the rate constant due to effects on motor binding to TMR-microtubules.

The donor quenching assays thus provide evidence for energy transfer during wild-type Ncd interactions with microtubules in the ATP-like state and NcdN600K interactions with microtubules without nucleotide. The FRET efficiency for wild-type Ncd with AMP·PNP was 24.9%, calculated from the photobleaching rate constant of the donor with and without acceptor (Eq. (5), Materials and methods). This corresponds to an estimated distance of 6 nm between the EGFP and TMR fluorophores on the microtubule surface (Fig. 4B). Similar values were observed for NcdN600K with no nucleotide ($E = 24.6\%$, $h = 6$ nm). Donor quenching was not observed for wild-type Ncd without nucleotide; the efficiency (bounded using the s.e.m.) was less than ~5%, corresponding to a distance of more than ~9 nm between the end of the stalk and microtubule surface.

4. Discussion

4.1. Ncd stalk movement detected by FRET

The mechanochemical cycle of the kinesin motors has been studied extensively, yet the question of when the power stroke occurs remains controversial. Here we examine a wild-type kinesin motor, Ncd, and a mutant that promotes rotation of the stalk, paralleling the structural change of the myosin lever arm that is thought to represent the primary mechanical component of the power stroke. The NcdN600K mutant binds tightly to microtubules and has been crystallized in a stalk-rotated conformation thought to represent a microtubule-bound motor (Yun et al 2003), indicating that this may represent a stable state of the mutant motor.

The stalk-rotated NcdN600K motor binds tightly to microtubules and shows energy transfer with or without nucleotide, including ADP, in acceptor photobleaching assays. Donor quenching assays indicate that, with no nucleotide, the stalk is ~6 nm from the microtubule. Wild-type Ncd binds to microtubules without added nucleotide, but does not show energy transfer without nucleotide by acceptor photobleaching or donor quenching assays. From the donor quenching assays, we estimate that the EGFP at the end of the stalk is more than ~9 nm from the microtubule. By contrast, acceptor photobleaching assays of wild-type Ncd bound to a non-hydrolysable ATP analogue, AMP·PNP, show evidence for FRET; donor quenching assays with AMP·PNP indicate that the stalk of wild-type Ncd is in close proximity, ~6 nm, to the microtubule, the same as NcdN600K with no added nucleotide.

We interpret the effects of the NcdN600K motor to mean that stalk rotation is allosterically linked to microtubule binding — NcdN600K binds tightly to microtubules and can be crystallized in a stalk-rotated conformation [11]. Another motor, NcdT436S, has also been crystallized in the same or similar conformation [12]; NcdT436S releases ADP faster than wild type with or without microtubules, but shows little or no change in microtubule-binding affinity. The effects of the NcdT436S and NcdN600K motors indicate that either weaker ADP binding or tighter microtubule binding promotes stalk rotation, providing evidence that movement of the stalk is correlated with ADP release and motor binding to microtubules. Wild-type Ncd has also been crystallized in a stalk-rotated conformation [11], but at lower resolution (~3.5 Å compared to 2.5 Å for NcdN600K and ~2.8 Å for NcdT436S), indicating that the NcdT436S and NcdN600K mutational changes might stabilize the conformation.

Further evidence that stalk rotation or other movement is coupled to microtubule binding is from 3D cryoEM reconstructions of wild-type dimeric Ncd bound to microtubules with ADP or without nucleotide, which show differences in the way the bound head interacts with tubulin and the position of the unbound head [30], indicating differences in the position of the stalk. Differences in the microtubule-bound Ncd-ADP conformation from the Ncd motor crystallized without microtubules are apparent by docking the crystal structures [31,32] into cryoEM reconstructions [13]. It is possible that Ncd-ADP has significant conformational flexibility, and indeed conformations in this nucleotide state show differences even among the crystallographic structures [33]. However, the evidence for allostery between microtubule binding and stalk rotation implies that microtubule binding and ADP release alter the distribution of states in favor of the more stalk-rotated states, even if they do not change the ensemble of states available. It is possible that the inferred first step in stalk rotation takes this form, but this shift would still be significant in the mechanochemical cycle of Ncd.

Microtubule binding and ADP release occur prior to ATP binding, a step in which the stalk of wild-type Ncd is close to the microtubule in FRET assays. The stalk may initiate rotation upon microtubule binding to allow one of the heads to bind to the microtubule. However, wild-type Ncd does not show FRET when bound to microtubules without nucleotide, indicating that the stalk has not rotated into a position close to the microtubule. The stalk of wild-type Ncd rotates into a position close to the microtubule only when the microtubule-bound motor binds the non-hydrolysable ATP analogue AMP·PNP.

4.2. Structural evidence for Ncd stalk rotation

Previous studies by cryoEM were interpreted to show that rotation of the stalk of the microtubule-bound Ncd motor is triggered by ATP binding [14,15]. The FRET data we report here are consistent with the interpretation that the stalk is rotated in the ATP state. The change in stalk orientation observed in the cryoEM studies may correspond to the second step of movement that we infer from our results, which may also be the more stable one or the one with a larger change in angle. Thus, despite the conclusion by others that ATP binding initiates stalk rotation, we propose that movement of the stalk is needed for the motor to bind to microtubules. If the previous hypothesis was correct that ATP binding triggers stalk rotation, altering ADP or microtubule binding by the motor would not be expected to change the motor conformation in crystal structures. Moreover, 3D cryoEM reconstructions of dimeric Ncd bound to microtubules with ADP or no nucleotide would be expected to show the same conformation as the motor-ADP free in solution. However, cryoEM reconstructions of Ncd bound to microtubules with ADP or no nucleotide show differences from Ncd-ADP crystal structures both in the bound and unbound heads, which result in poor fits of the crystal structures into the cryoEM density maps [13,30]. Thus, we propose that stalk movement is initiated when the Ncd motor binds microtubules and releases ADP, and rotation is completed upon ATP binding, rather than triggered by ATP binding.

The NcdN600K crystal structure (PDB 1N6M) with its ~75° stalk rotation provides structural evidence that the stalk undergoes a large rotation during the force-generating cycle [11]. The angle was estimated by superposing the NcdN600K rotated head in chain B with one of the two heads of an unrotated Ncd-ADP structure (PDB 1CZ7), and measuring the difference in angle between the stalks [11].

The end of the NcdN600K stalk is ~6 nm from the microtubule based on our FRET data, corresponding to a rotation of ~70° from a vertical position. This is consistent with the ~75° rotation in the NcdN600K crystal structure compared to a previous motor-ADP structure, assuming that the unrotated motor-ADP represents the motor as it binds to a microtubule. We also estimated the distance the end of the stalk in the NcdN600K crystal structure would be from the microtubule surface by fitting a plane by least squares through C_α of several residues in helices α4 and α5 of the microtubule-binding site of the rotated head in chain B and calculating the distance between the plane and C_α of M292 at the end of the stalk. The distance was 5.9 nm, in agreement with the distance of 6 nm from our FRET data.

The angle the stalk rotates during force generation would be greater if the stalk is initially tilted toward the microtubule plus end when the motor binds to a microtubule, as suggested by cryoEM studies [14,15]. However, the cryoEM maps that were interpreted to show this are no-nucleotide maps into which an Ncd-ADP crystal structure was docked, and the Ncd-ADP motor is probably not in the correct conformation for the no-nucleotide state. There are no cryoEM maps of Ncd-ADP bound to microtubules in which the end of the stalk is visible, so the cryoEM data do not provide information regarding the position of the stalk in the initial microtubule-bound state or whether the initial position differs from the stable no-nucleotide as we proposed based on previous structural evidence.

4.3. Stalk rotation and Ncd step size

Rotation of the Ncd stalk could displace an attached load along the microtubule to produce the steps by the motor observed in laser-trap assays [34] (Fig. 6). Movement by the Ncd motor is not always parallel to the microtubule long axis, as observed for kinesin-1 [35]; instead Ncd has been hypothesized to take off-axis steps that vary in frequency, causing microtubules bound to the motor attached to a surface to rotate as they glide [36]. Steps, or changes in the center of mass of the load, driven by Ncd stalk movement or rotation, may thus show an off-axis component, differing from kinesin-1 (Fig. 6). An initial tilt of the stalk towards the microtubule plus end could also affect the step size, depending on the angle of tilt, since a component of the stalk movement parallel to the microtubule long axis is dependent on the angle of tilt.

If the stalk movement is parallel to the microtubule long axis, the step size would be equal to the displacement of the load along the microtubule, d. If the step is not parallel to the microtubule axis, the step size is related to d, as shown (Fig. 6A). The step size of Ncd is predicted to be greater than the 8-nm step observed for kinesin-1, where d for each

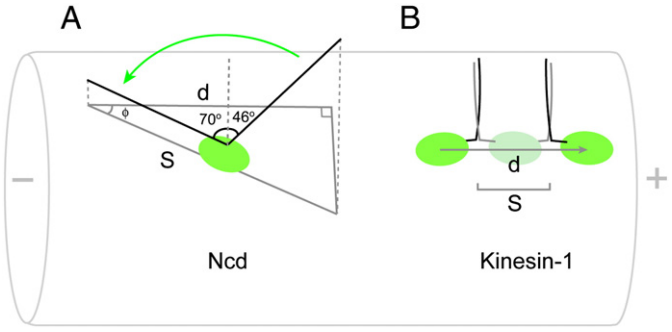

Fig. 6. Model for motor steps. (A) Ncd steps are produced by rotation or other movement of the stalk (arrow) relative to the bound head (oval). A ~70° rotation was inferred from FRET data reported here (see Discussion). A tilt of 46° towards the plus end was measured from a cryoEM docking [14,15]. Ncd frequently steps off-axis relative to the microtubule long axis [34], as shown. Step size is $S = l(\sin\theta_1 + \sin\theta_2)$, where l = stalk length, and displacement along the microtubule is $d = S\cos\phi$ (B) Kinesin-1 alternatively moves its two heads to a new binding site along the microtubule to produce steps [42–45]; steps are parallel to the microtubule axis [35], step size is 8 nm [46] and displacement of each head along the microtubule is d = 16 nm.

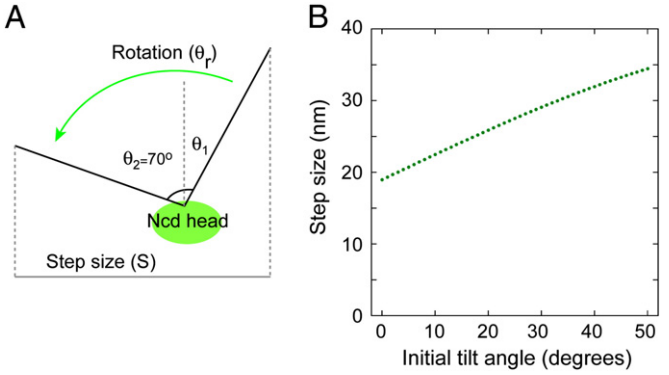

Fig. 7. Effect of initial stalk position on step size. (A) Movement of the stalk from an initial position tilted by an angle θ_1 toward the microtubule plus end. The stalk (black line) rotates through an angle $\theta_r = \theta_1 + \theta_2$, where $\theta_2 \approx 70°$ and $\theta_1 = 0$ if the motor binds to the microtubule with the stalk perpendicular to the microtubule. For illustration, the plane of movement is parallel to the microtubule long axis and only the bound head of the motor is shown. The dashed gray lines are perpendicular to the microtubule surface (not shown). (B) Step size (S), or displacement of the load attached to the end of the stalk along the microtubule (d) as a function of the initial tilt angle θ_1, given a stalk rotation of $\theta_r = \theta_1 + 70°$ and stalk length l = 20.2 nm as predicted for full-length Ncd, assuming movement of the stalk parallel to the microtubule long axis. Step size is equal to displacement along the microtubule for steps parallel to the microtubule long axis, and $S = d = l(\sin\theta_1 + \sin\theta_2)$.

head is 16 nm (Fig. 6B) — the steps of full-length Ncd with a stalk of l = 20.2 nm could be as large as 33.5 nm or more, depending on the initial tilt towards the plus (or minus) end. The step size for full-length Ncd, assuming a stalk rotation of $\theta_r = \theta_1 + \theta_2$, where $\theta_2 = 70°$, and movement occurs in a plane parallel to the microtubule long axis, is shown as a function of the initial tilt angle θ_1 (Fig. 7). The Ncd step size is not constrained by motor binding sites along the microtubule as it is for kinesin-1; instead it is limited by the stalk length and angle of stalk movement, which, in the spindle, could be influenced by motor:motor interactions [37] or interactions with other proteins.

The ability to modulate step size upon interaction with other proteins would allow Ncd to function effectively over a wide range of motor densities, explaining its versatility in spindle function [38]. This contrasts with kinesin-1, a highly processive motor that appears adapted to permit single or a few molecules to move cargo forward at a rapid velocity, rather than adjusting force production to changes in motor density.

4.4. Two-state model for Ncd stalk movement

Initiation of Ncd stalk movement by microtubule binding and completion of stalk rotation upon ATP binding are consistent with the observation of a two-step working stroke for wild-type full-length Ncd by laser-trap analysis [26], although the steps of ~1–2 nm and ~9 nm that were reported are smaller than the 19-nm displacement predicted for a 70° rotation of the stalk from a vertical position — a step of ~9 nm corresponds to an angle change of ~26°, based on a 20.2-nm stalk length for full-length Ncd (see Materials and methods). The first step was attributed to a possible artifact caused by the experimental geometry [26]. The smaller than predicted size of the second larger step might be due to nonspecific adsorption of the motor to the bead in the laser-trap assays, which could reduce the stalk length, the occurrence of several small steps prior to the larger one that occurs upon ATP binding, or motor binding to a microtubule with the stalk partially rotated from a perpendicular position.

The α-helical coiled-coil stalk of Ncd and other kinesin motors may act like the myosin lever arm to produce force and displace the motor along its filament. The rotation by the Ncd stalk and myosin lever arm to produce force appears to differ from the dyneins [39], where a swing of an α-helix-rich N-terminal structure termed the "linker" across the motor domain [40], coupled to a shift in heptad registry of the coiled-coil stalk that joins the microtubule-binding

region to the motor [41], could drive movement. Our proposal here that Ncd stalk movement is initiated by microtubule binding and rotation is completed upon ATP binding is reminiscent of the two-step working stroke of myosin I [8]. Despite the structural homology between the kinesins and myosins, an analogous power stroke is not entirely expected, since interactions of the motors with their cytoskeletal filaments differ at several steps of the nucleotide hydrolysis cycle. We thus propose that the conformational changes that drive kinesin-14 motor movement along microtubules are triggered by microtubule binding and completed upon ATP binding. The full nature of these movements remains to be elucidated.

4.5. Conclusions

The wild-type kinesin-14 motor Ncd and a mutant that affects stalk rotation were examined in FRET assays to determine the nucleotide state in which the stalk undergoes movement, producing force and a displacement or step by the motor. Previous crystal structures of mutants that alter ADP or microtubule binding by the motor, together with cryoEM reconstructions of dimeric Ncd bound to microtubules in different nucleotide states imply that movement of the stalk is required for the motor to bind to microtubules. The NcdN600K mutant has been crystallized in a stalk-rotated conformation; it binds tightly to microtubules and showed FRET in all three nucleotide states that we tested, showing that FRET is correlated with rotation of the stalk. Wild-type Ncd showed FRET when bound to microtubules with a non-hydrolysable ATP analogue, but not without nucleotide. We interpret these results, together with the effects of the NcdN600K mutant, to mean that the Ncd stalk initiates movement when the motor binds to microtubules and rotates close to the microtubule upon binding to ATP. The two-state displacement of the stalk is predicted to produce a step by Ncd that greatly exceeds the size of the kinesin-1 step.

Acknowledgments

We thank Gordon Hammes for helpful discussions and the use of a TIRF microscope. This work was supported by a grant to S.A.E. from the NIH (NIGMS GM046225). M.A.H. is a National Defense Science and Engineering Graduate Fellow and James B. Duke Scholar.

References

[1] J. Howard, Mechanics of Motor Proteins and the Cytoskeleton, Sinauer Associates, Inc., Sunderland, MA, 2001.
[2] I. Rayment, H. Holden, M. Whittaker, C.B. Yohn, M. Lorenz, K.C. Holmes, R.A. Milligan, Structure of the actin–myosin complex and its implications for muscle contraction, Science 261 (1993) 58–65.
[3] T.Q.P. Uyeda, P.D. Abramson, J.A. Spudich, The neck region of the myosin motor domain acts as a lever arm to generate movement, Proc. Natl Acad. Sci. USA 93 (1996) 4459–4464.
[4] Z. Bryant, D. Altman, J.A. Spudich, The power stroke of myosin VI and the basis of reverse directionality, Proc. Natl Acad. Sci. USA 104 (2007) 772–777.
[5] I. Rayment, W.R. Rypniewski, K. Schmidt-Bäse, R. Smith, D.R. Tomchick, M.M. Benning, D.A. Winkelmann, G. Wesenberg, H.M. Holden, Three-dimensional structure of myosin subfragment-1: a molecular motor, Science 261 (1993) 50–58.
[6] R. Dominguez, Y. Freyzon, K.M. Trybus, C. Cohen, Crystal structure of a vertebrate smooth muscle myosin motor domain and its complex with the essential light chain: visualization of the pre-power stroke state, Cell 94 (1998) 559–571.
[7] Y. Suzuki, T. Yasunaga, R. Ohkura, T. Wakabayashi, K. Sutoh, Swing of the lever arm of a myosin motor at the isomerization and phosphate-release steps, Nature 396 (1998) 380–383.
[8] C. Veigel, L.M. Coluccio, J.D. Jontes, J.C. Sparrow, R.A. Milligan, J.E. Molloy, The motor protein myosin-I produces its working stroke in two steps, Nature 398 (1999) 530–533.
[9] M. Irving, G. Piazzesi, L. Lucii, Y.B. Sun, J.J. Harford, I.M. Dobbie, M.A. Ferenczi, M. Reconditi, V. Lombardi, Conformation of the myosin motor during force generation in skeletal muscle, Nat. Struct. Biol. 7 (2000) 482–485.
[10] E. Toprak, J. Enderlein, S. Syed, S.A. McKinney, R.G. Petschek, T. Ha, Y.E. Goldman, P.R. Selvin, Defocused orientation and position imaging (DOPI) of myosin V, Proc. Natl Acad. Sci. USA 103 (2006) 6495–6499.
[11] M. Yun, C.E. Bronner, C.-G. Park, S.-S. Cha, H.-W. Park, S.A. Endow, Rotation of the stalk/neck and one head in a new crystal structure of the kinesin motor protein, Ncd, EMBO J. 22 (2003) 5382–5389.
[12] E. Heuston, C.E. Bronner, F.J. Kull, S.A. Endow, A kinesin motor in a force-producing conformation, BMC Struct. Biol. 10 (2010) 19.
[13] K. Hirose, J. Löwe, M. Alonso, R.A. Cross, L.A. Amos, Congruent docking of dimeric kinesin and ncd into three-dimensional electron cryomicroscopy maps of microtubule–motor ADP complexes, Mol. Biol. Cell 10 (1999) 2063–2074.
[14] T.G. Wendt, N. Volkmann, G. Skiniotis, K.N. Goldie, J. Müller, E. Mandelkow, A. Hoenger, Microscopic evidence for a minus-end-directed power stroke in the kinesin motor ncd, EMBO J. 21 (2002) 5969–5978.
[15] N.F. Endres, C. Yoshioka, R.A. Milligan, R.D. Vale, A lever-arm rotation drives motility of the minus-end-directed kinesin Ncd, Nature 439 (2006) 875–878.
[16] G.H. Patterson, S.M. Knobel, W.D. Sharif, S.R. Kain, D.W. Piston, Use of the green fluorescent protein and its mutants in quantitative fluorescence microscopy, Biophys. J. 73 (1997) 2782–2790.
[17] J. Helenius, G. Brouhard, Y. Kalaidzidis, S. Diez, J. Howard, The depolymerizing kinesin MCAK uses lattice diffusion to rapidly target microtubule ends, Nature 441 (2006) 115–119.
[18] P.T.R. Rajagopalan, Z. Zhang, L. McCourt, M. Dwyer, S.J. Benkovic, G.G. Hammes, Interaction of dihydrofolate reductase with methotrexate: ensemble and single-molecule kinetics, Proc. Natl Acad. Sci. USA 99 (2002) 13481–13486.
[19] D.R. Kellogg, T.J. Mitchison, B.M. Alberts, Behaviour of microtubules and actin filaments in living *Drosophila* embryos, Development 103 (1988) 675–686.
[20] A. Hyman, D. Drechsel, D. Kellogg, S. Salser, K. Sawin, P. Steffen, L. Wordeman, T. Mitchison, Preparation of modified tubulins, Meth. Enzymol. 196 (1991) 478–485.
[21] T. Förster, Transfer mechanisms of electronic excitation, Discuss. Faraday Soc. 27 (1959) 7–16.
[22] G.H. Patterson, D.W. Piston, B.G. Barisas, Förster distances between green fluorescent protein pairs, Anal. Biochem. 284 (2000) 438–440.
[23] B.B. Hopkins, N.O. Reich, Simultaneous DNA binding, bending, and base flipping: evidence for a novel M.EcoRI methyltransferase–DNA complex, J. Biol. Chem. 279 (2004) 37049–37060.
[24] R.C. Patel, D.C. Lange, Y.C. Patel, Photobleaching fluorescence resonance energy transfer reveals ligand-induced oligomer formation of human somatostatin receptor subtypes, Methods 27 (2002) 340–348.
[25] B.A. Baird, U. Pick, G.G. Hammes, Structural investigation of reconstituted chloroplast ATPase with fluorescence measurements, J. Biol. Chem. 254 (1979) 3818–3825.
[26] M.J. deCastro, R.M. Fondecave, L.A. Clarke, C.F. Schmidt, R.J. Stewart, Working strokes by single molecules of the kinesin-related microtubule motor ncd, Nat. Cell Biol. 2 (2000) 724–729.
[27] H. Song, S.A. Endow, Decoupling of nucleotide- and microtubule-binding in a kinesin mutant, Nature 396 (1998) 587–590.
[28] I.M.-T.C. Crevel, A. Lockhart, R.A. Cross, Weak and strong states of kinesin and ncd, J. Mol. Biol. 257 (1996) 66–76.
[29] D.D. Hackney, The kinetic cycles of myosin, kinesin, and dynein, Annu. Rev. Physiol. 58 (1996) 731–750.
[30] K. Hirose, R.A. Cross, L.A. Amos, Nucleotide-dependent structural changes in dimeric NCD molecules complexed to microtubules, J. Mol. Biol. 278 (1998) 389–400.
[31] E.P. Sablin, F.J. Kull, R. Cooke, R.D. Vale, R.J. Fletterick, Crystal structure of the motor domain of the kinesin-related motor ncd, Nature 380 (1996) 555–559.
[32] E.P. Sablin, R.B. Case, S.C. Dai, C.L. Hart, A. Ruby, R.D. Vale, R.J. Fletterick, Direction determination in the minus-end-directed kinesin motor ncd, Nature 395 (1998) 813–816.
[33] F. Kozielski, S. De Bonis, W.P. Burmeister, C. Cohen-Addad, R.H. Wade, The crystal structure of the minus-end-directed microtubule motor protein ncd reveals variable dimer conformations, Structure 7 (1999) 1407–1416.
[34] S.A. Endow, H. Higuchi, A mutant of the motor protein kinesin that moves in both directions on microtubules, Nature 406 (2000) 913–916.
[35] S. Ray, E. Meyhöfer, R.A. Milligan, J. Howard, Kinesin follows the microtubule's protofilament axis, J. Cell Biol. 121 (1993) 1083–1093.
[36] R.A. Walker, E.D. Salmon, S.A. Endow, The *Drosophila claret* segregation protein is a minus-end directed motor molecule, Nature 347 (1990) 780–782.
[37] C.J. Sciambi, D.J. Komma, H.N. Sköld, K. Hirose, S.A. Endow, A bidirectional kinesin motor in live *Drosophila* embryos, Traffic 6 (2005) 1036–1046.
[38] M.A. Hallen, S.A. Endow, Anastral spindle assembly: a mathematical model, Biophys. J. 97 (2009) 2191–2201.
[39] H. Ueno, T. Yasunaga, C. Shingyoji, K. Hirose, Dynein pulls microtubules without rotating its stalk, Proc. Natl Acad. Sci. USA 105 (2008) 19702–19707.
[40] A.J. Roberts, N. Numata, M.L. Walker, Y.S. Kato, B. Malkova, T. Kon, R. Ohkura, F. Arisaka, P.J. Knight, K. Sutoh, et al., AAA+ ring and linker swing mechanism in the dynein motor, Cell 136 (2009) 485–495.
[41] A.P. Carter, J.E. Garbarino, E.M. Wilson-Kubalek, W.E. Shipley, C. Cho, R.A. Milligan, R.D. Vale, I.R. Gibbons, Structure and functional role of dynein's microtubule-binding domain, Science 322 (2008) 1691–1695.
[42] K. Kaseda, H. Higuchi, K. Hirose, Alternate fast and slow stepping of a heterodimeric kinesin molecule, Nat. Cell Biol. 5 (2003) 1079–1082.
[43] C.L. Asbury, A.N. Fehr, S.M. Block, Kinesin moves by an asymmetric hand-over-hand mechanism, Science 302 (2003) 2130–2134.
[44] A. Yildiz, M. Tomishige, R.D. Vale, P.R. Selvin, Kinesin walks hand-over-hand, Science 303 (2004) 676–678.
[45] H. Higuchi, C.E. Bronner, H.W. Park, S.A. Endow, Rapid double 8-nm steps by a kinesin mutant, EMBO J. 23 (2004) 2993–2999.
[46] K. Svoboda, C.F. Schmidt, B.J. Schnapp, S.M. Block, Direct observation of kinesin stepping by optical trapping interferometry, Nature 365 (1993) 721–727.